Evaluation of Current Ripple Amplitude in Five-Phase PWM Voltage Source Inverters

Gabriele Grandi, Jelena Loncarski
Department of Electrical, Electronic and Information Engineering
Alma Mater Studiorum - University of Bologna, Italy
gabriele.grandi@unibo.it, jelena.loncarski2@unibo.it

***Abstract*—Multiphase systems are nowadays considered for various industrial applications. Numerous PWM schemes for multiphase voltage source inverters with sinusoidal outputs have been developed, but no detailed analysis of the impact of these modulation schemes on the output peak-to-peak current ripple amplitude has been reported. Determination of current ripple in five-phase PWM voltage source inverters is important for both design and control purposes. This paper gives the complete analysis of the peak-to-peak current ripple distribution over a fundamental period. In particular, peak-to-peak current ripple amplitude is analytically determined as a function of the modulation index, and a simplified expression to get its maximum value is carried out. Reference is made to centered symmetrical PWM, being the most simple and effective solution to maximize the dc bus utilization, leading to a nearly-optimal modulation to minimize the rms of current ripple. However, the analysis can be easily extended to either discontinuous or asymmetrical modulation, both carrier-based and space vector PWM. The analytical developments for all the different sub-cases are verified by numerical simulations.**

Keywords—Output current ripple; multiphase drives; space vector PWM; voltage source inverter; switching sequence.

I. INTRODUCTION

Multiphase motor drives have many advantages over the traditional 3-phase motor drives. Among them are ability to reduce the amplitude and to increase the frequency of torque pulsations, by reducing the rotor harmonic current losses and lowering the dc link current harmonics. In addition, owing to their redundant structure, multiphase motor drives improve the system reliability [1]-[4].

In general, the problems related to high-power applications can be overcome by the increase of the number of phases, which is considered as a viable solution. In the last decades, multilevel inverter-fed 3-phase ac systems have emerged as a promising solution in achieving high power ratings with voltage limited devices. The use of multiphase inverters together with multiphase ac machines similarly has been recognized as a viable approach to obtain high power ratings with current limited devices.

The behavior of the multiphase systems can be represented by the space vector theory, as a natural extension of the traditional 3-phase space vector transformation, leading to an elegant and effective vectorial approach in multiple α–β planes [5]. The space vectors can be usefully adopted for the modulation of multiphase inverters. The space vector modulation (SVM) for 5-phase voltage source inverters (VSIs) has been developed in [6]-[9]. In general, for any number of phases, it has been proved that the SV-PWM provides the same switching pattern such as the carried-based (CB) PWM with a proper common-mode voltage injection into the modulating signals [10]. In particular, centering the modulating signals corresponds to equally share the null vector between the two null configurations.

Recent studies about rms output current ripple in multiphase motor drives are given in [11]-[13], considering a 5-phase system. In [11] the optimal value of the common-mode voltage injection in CB-PWM has been analytically determined to minimize the rms current ripple in each switching period. Furthermore, it is shown that the strategy called SV-PWM, corresponding to centered and symmetric modulation, has a nearly-optimal behavior in term of the current ripple rms. In [12] it is shown that output current ripple rms cannot be minimized by injection of fifth harmonic and its odd multiples, but it is also pointed out that, from the practical point of view, differences in current ripple rms are relatively small considering sinusoidal PWM and SV-PWM. In [13] the two SV-PWM techniques with 4 large, and 2 large and 2 middle vectors are compared in terms of THD of the current and voltage with established correlations between the flux HDF and the current THD, and squared rms current ripple. In [14] an attempt to evaluate the output rms current ripple of a 5-phase inverter has been reported, on the basis of polygon load connection and phase variables in the original domain, without the need to use space-vector theory. However, only a single (adjacent) polygon connection has been used, and the output current-ripple rms does not represent the total output current ripple [15].

The importance of the peak-to-peak current ripple evaluation in addition to the rms analysis is recognized in [16], where the ripple amplitude is investigated for 3-phase PWM inverters. A similar investigation is presented in [17], with detailed analytical expressions of a peak-to-peak current ripple distribution over the fundamental period. Simple and effective expressions to determine the maximum and the minimum of the current ripple amplitude in the fundamental period are also given.

For the practical usage, the knowledge of the peak-to-peak current ripple distribution can be useful to determine the output voltage distortion due to the switch dead-time in case of output currents with high ripple by determining their multiple zero-crossing intervals [18]. The effects of high-ripple currents on dead-time with adaptive compensation are studied in

[19] and [20] as well, where the knowledge of peak-to-peak current ripple was of interest but it has not been properly addressed. Another example of application is referred to hysteresis current controllers and variable switching frequency PWM, for single-phase [21] and three-phase inverters [22], [23].

Furthermore, the peak-to-peak current ripple amplitude, in addition to the fundamental current component, is useful to determine the absolute current peak, affecting the thresholds of protection systems and the design of power components.

In this paper, the method to determine the peak-to-peak current ripple proposed in [17] for 3-phase VSIs is revised and extended to the case of 5-phase VSIs. The analysis is developed with reference to symmetrical centered switching patterns, generated either by CB- or SV-PWM. Detailed analytical expressions of the peak-to-peak current ripple amplitude distribution over a fundamental period are given as function of the modulation index. Furthermore, maximum of the peak-to-peak current ripple is evaluated introducing simplified and effective expression. The instantaneous current ripple is introduced for a generic balanced 5-phase load consisting of a series RL impedance with an ac backemf (RLE). All the analytical developments are verified by numerical simulations on a realistic circuit model of the inverter-load system, implemented by the Simulink tool of Matlab.

II. Evaluation of Peak-to-Peak Current Ripple

A. Load model and current ripple definitions

Basic circuit scheme for inverter supplying a RLE load is represented in Fig. 1. The voltage equation can be written for each phase as

$$v(t) = R\,i(t) + L\frac{di}{dt} + v_g(t)\,. \tag{1}$$

By averaging (1) over the switching period T_s leads to

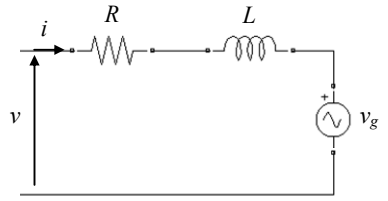

Fig. 1. Basic RLE circuit model for one phase.

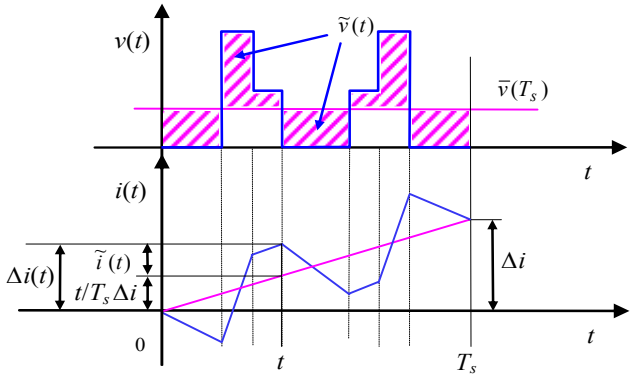

Fig. 2. Details of a generic output voltage and current ripple in the switching period.

$$\bar{v}(T_s) = R\,\bar{i}(T_s) + L\frac{\Delta i}{T_s} + \bar{v}_g(T_s)\,, \tag{2}$$

being $\Delta i = i(T_s) - i(0)$. (3)

The alternating component of inverter voltage can be written by introducing the average over the switching period as

$$\tilde{v}(t) = v(t) - \bar{v}(T_s)\,. \tag{4}$$

By introducing (1) and (2) in (4) leads to

$$\tilde{v}(t) = R\left[i(t) - \bar{i}(T_s)\right] + L\left[\frac{di}{dt} - \frac{\Delta i}{T_s}\right] + \left[v_g(t) - \bar{v}_g(T_s)\right]. \tag{5}$$

The expression of alternating voltage component can be simplified since the first and the third (last) term in (5) are negligible with respect to the second term, leading to

$$\tilde{v}(t) \cong L\left[\frac{di}{dt} - \frac{\Delta i}{T_s}\right]. \tag{6}$$

The current variation in the sub-period [0 – t], also depicted in Fig. 2, can be calculated from (6) as

$$\Delta i(t) \cong \frac{1}{L}\int_0^t \tilde{v}(t)dt + \frac{t}{T_s}\Delta i\,. \tag{7}$$

Eq. (7) allows defining the instantaneous current ripple as

$$\tilde{i}\,(t) = \Delta i(t) - \frac{t}{T_s}\Delta i \cong \frac{1}{L}\int_0^t \tilde{v}(t)dt\,. \tag{8}$$

Finally, the peak-to-peak current ripple amplitude can be calculated as

$$\tilde{i}_{pp} = max\left\{\tilde{i}\,(t)\right\}_0^{T_s} - min\left\{\tilde{i}\,(t)\right\}_0^{T_s}. \tag{9}$$

B. Multiple space vectors and PWM equations

Multiple space vectors are introduced to represent voltage and current phase quantities in multiphase systems [5]. For the 5-phase system $\{x_1, x_2, x_3, x_4, x_5\}$, the two space vectors $\boldsymbol{x}_1$ and $\boldsymbol{x}_3$ lie in the two planes α_1–β_1 and α_3–β_3, respectively, and are expressed as

$$\begin{cases} \boldsymbol{x}_1 = \dfrac{2}{5}\left[x_1 + x_2\boldsymbol{\alpha} + x_3\boldsymbol{\alpha}^2 + x_4\boldsymbol{\alpha}^3 + x_5\boldsymbol{\alpha}^4\right] \\ \boldsymbol{x}_3 = \dfrac{2}{5}\left[x_1 + x_2\boldsymbol{\alpha}^3 + x_3\boldsymbol{\alpha} + x_4\boldsymbol{\alpha}^4 + x_5\boldsymbol{\alpha}^2\right], \\ x_0 = \dfrac{1}{5}\left[x_1 + x_2 + x_3 + x_4 + x_5\right] \end{cases} \tag{10}$$

being $\boldsymbol{\alpha} = exp(j2\pi/5)$ and the x_0 the zero-sequence component, always null in case of balanced systems.

The inverse transformation of (10) is

$$x_k = x_0 + \boldsymbol{x}_1 \cdot \boldsymbol{\alpha}^{(k-1)} + \boldsymbol{x}_3 \cdot \boldsymbol{\alpha}^{3(k-1)}\,,\ k = 1, 2, \ldots, 5. \tag{11}$$

With reference to a 5-phase VSI supplied by the dc voltage V_{dc}, the output space voltage vectors can be written as function of the 5 switching leg states $S_k = [0, 1]$ as

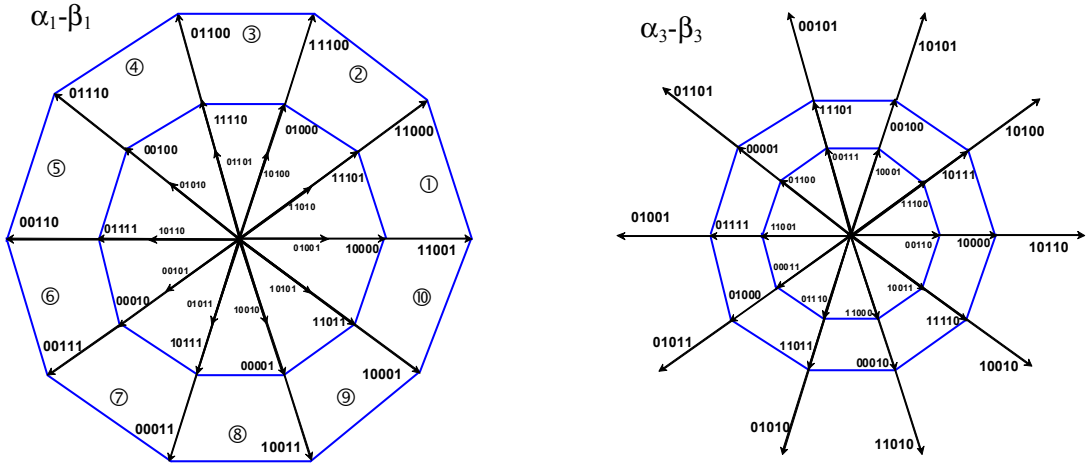

Fig. 3. Space vector diagrams of inverter output voltage in the planes α_1-β_1 and α_3-β_3 .

$$\begin{cases} \boldsymbol{v}_1 = \dfrac{2}{5} V_{dc}\left[S_1 + S_2\boldsymbol{\alpha} + S_3\boldsymbol{\alpha}^2 + S_4\boldsymbol{\alpha}^3 + S_5\boldsymbol{\alpha}^4\right] \\ \boldsymbol{v}_3 = \dfrac{2}{5} V_{dc}\left[S_1 + S_2\boldsymbol{\alpha}^3 + S_3\boldsymbol{\alpha} + S_4\boldsymbol{\alpha}^4 + S_5\boldsymbol{\alpha}^2\right] \end{cases} \tag{12}$$

The space vector diagrams representing all possible switch configurations in planes α_1–β_1 and α_3–β_3 are given in Fig. 3.

The SV-PWM of 5-phase inverters is based on the determination of application times of active and null inverter voltage vectors $\boldsymbol{v}_1$ and $\boldsymbol{v}_3$ in every switching period T_s. In the case of symmetrical SV-PWM, the sequence is determined in T_s /2 and symmetrically repeated in the next half switching period. By equally sharing the application time of the null voltage vector between the switch configurations 00000 and 11111, the so called "centered" switching pattern is realized. This SV-PWM provides the same switching pattern such as the CB-PWM when a "min/max centering" common-mode voltage is injected into the modulating signals [10].

As result of this modulation, the average of the inverter output voltage $\bar{v}(T_s)$ corresponds to the reference voltage v^*, for each phase.

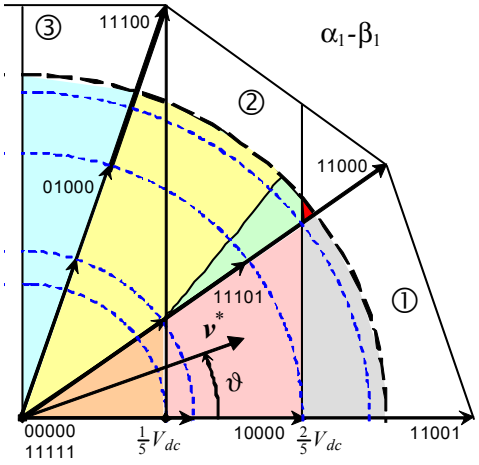

Fig. 4. Space vector diagram of inverter output voltage on plane α_1–β_1 in the range ϑ = [0, 90°]. Outer dashed circle is the modulation limit, $m_{max} \approx 0.526$. Colored areas represent different equations to determine the current ripple.

In the case of sinusoidal balanced output voltages supplying a balanced load, the zero-sequence component is null. Introducing the modulation index $m = V^*/V_{dc}$, the reference space voltage vectors become

$$\begin{cases} \boldsymbol{v}_1^* = \boldsymbol{v}^* = m V_{dc} e^{j\vartheta} \\ \boldsymbol{v}_3^* = 0 . \end{cases} \tag{13}$$

In this case, SV modulation is quarter-wave symmetric, and it can be analyzed in the range [0, π/2] of the phase angle $\vartheta = \omega t$. With reference to Fig. 4, the sectors ① and ② are considered for $0 \le \vartheta \le \pi/5$ and $\pi/5 \le \vartheta \le 2\pi/5$, respectively, and the half of sector ③ is considered for $2\pi/5 \le \vartheta \le \pi/2$.

For sector ① the application times of the switch configurations involved in the modulation sequence from 00000 to 11111 in the half period $T_s/2$ can be determined as [6]

$$t_1 = m T_s K_1 \sin(\pi/5 - \vartheta) , \qquad \{10000\} \tag{14}$$

$$t_2 = m T_s K_3 \sin\vartheta , \qquad \{11000\} \tag{15}$$

$$t_3 = m T_s K_3 \sin(\pi/5 - \vartheta) , \qquad \{11001\} \tag{16}$$

$$t_4 = m T_s K_1 \sin\vartheta , \qquad \{11101\} \tag{17}$$

$$t_0 = \frac{T_s}{2} - (t_1 + t_2 + t_3 + t_4) = \\ = \frac{T_s}{2}\left[1 - m\left(1 + \cos\frac{\pi}{5}\right)\cos\vartheta - mK_1 \sin\vartheta\right], \quad \begin{matrix}\{00000\} \\ \{11111\}\end{matrix} \tag{18}$$

being

$$\begin{cases} K_1 = \sin\dfrac{\pi}{5} \cong 0.588 \\ K_3 = \sin\dfrac{3\pi}{5} \cong 0.951 . \end{cases} \tag{19}$$

Equations (14)-(18) can be extended to any sector k by replacing the phase angle ϑ by ϑ–$(k\text{-}1)\pi/5$, k = 1, 2, …, 10.

Note that the modulation limit is $m \le m_{\max} \approx 0.526$, according to the generalized expression given in [24] for n phases, $m_{\max} = [2\cos(\pi/2n)]^{-1}$.

C. *Ripple evaluation*

Due to the symmetry among all phases in the considered case of sinusoidal balanced currents, only the first phase is examined in the following analysis. In terms of multiple space vectors, the phase variables are given by (11). For the first phase, it results in the projection of the two space vectors on the real axes. In particular, introducing (13) in (11), the average output voltage of the first phase is given by

$$\bar{v}(T_s) = v^* = \Re e\{\boldsymbol{v}_1^*\} + \Re e\{\boldsymbol{v}_3^*\} = mV_{dc}\cos\vartheta\,. \tag{20}$$

By introducing (20) in (4), and calculating $v(t)$ by (11) and (12), the alternating component of inverter output voltage of the first phase can be written as

$$\tilde{v}(t) = \left[S_1 - \frac{1}{5}\left(S_1 + S_2 + S_3 + S_4 + S_5\right)\right]V_{dc} - mV_{dc}\cos\vartheta\,. \tag{21}$$

In order to evaluate the current ripple in the whole phase angle range $0 < \vartheta < \pi/2$, the three main cases corresponding to the three sectors depicted in Fig. 4 should be considered. Additional sub-cases, also determined by the value of modulation index are identified in Fig. 4 with different colors.

The current ripple is depicted in a separate diagram for each sector, from Fig. 5 to Fig. 7. In general, the ripple shows 2 peaks in the switching period (2 positive and the symmetric negative). For all cases, one peak always bigger than the other in the considered sector, for any specific range of $m\cos\vartheta$, due to current slopes and application times. The only exception is in the second sector ②, where either one or the other peak is bigger depending on the values of m and ϑ.

1) Evaluation in the first sector

Considering sector ①, $0 \le \vartheta \le \pi/5$, three different sub-cases can be distinguished: $0 \le m\cos\vartheta \le 1/5$, $1/5 \le m\cos\vartheta \le 2/5$, and $2/5 \le m\cos\vartheta \le m_{\max}\cos\vartheta < 3/5$. All this sub-cases are represented in Fig. 5.

The sub-case $0 \le m\cos\vartheta \le 1/5$ (orange area in Fig. 4) is considered in diagram ❶ of Fig. 5, where the current ripple $\tilde{i}$ and its peak-to-peak value $\tilde{i}_{pp}$ are depicted, together with the instantaneous output voltage $v(t)$. In this case, according to Fig. 5, $\tilde{i}_{pp}$ can be evaluated by (8), (9) and (21) considering switch configurations 11111 or 00000 with the corresponding application interval t_0, leading to

$$\tilde{i}_{pp} = \frac{1}{L}\{mV_{dc}\cos\vartheta\, t_0\}. \tag{22}$$

Peak-to-peak current ripple can also be expressed as

$$\tilde{i}_{pp} = \frac{V_{dc}T_s}{2L}r(m,\vartheta)\,, \tag{23}$$

being $r(m,\vartheta)$ the normalized peak-to-peak current ripple amplitude. Introducing the duty-cycle $\delta_k = t_k/T_s/2$ leads to

$$r(m,\vartheta) = m\cos\vartheta\,\delta_0\,. \tag{24}$$

The sub-case $1/5 \le m\cos\vartheta \le 2/5$ (pink area in Fig. 4) is depicted in diagram ❷ of Fig. 5. In this case $\tilde{i}_{pp}$ can be evaluated considering the switch configurations 11111 and 11101, with corresponding application intervals $t_0/2$ and t_4, leading to

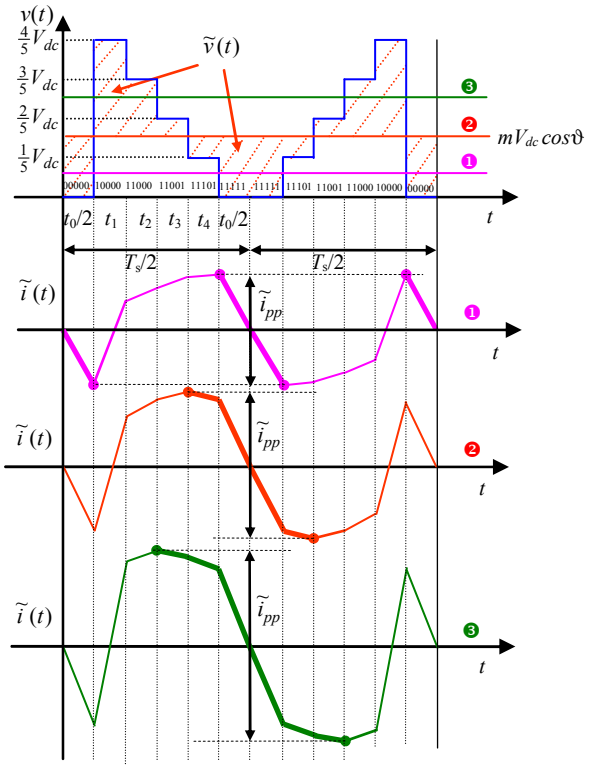

Fig. 5. Output voltage and current ripple in one switching period for sector ①, $0 \le \vartheta \le \pi/5$.

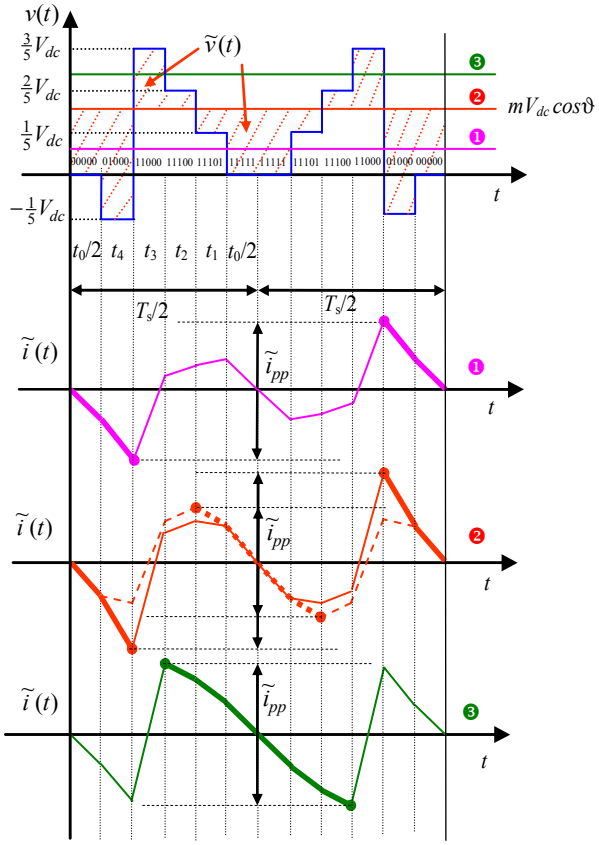

Fig. 6. Output voltage and current ripple in one switching period for sector ②, $\pi/5 \le \vartheta \le 2\pi/5$.

$$\tilde{i}_{pp} = \frac{2}{L}\left\{ m V_{dc} \cos\vartheta \frac{t_0}{2} + \left(m V_{dc} \cos\vartheta - \frac{V_{dc}}{5} \right) t_4 \right\}. \quad (25)$$

Normalizing as in (23) and introducing the duty-cycles $\delta_k = t_k/T_s/2$, the normalized current ripple becomes

$$r(m,\vartheta) = m\cos\vartheta\,\delta_0 + 2\left(m\cos\vartheta - \frac{1}{5} \right)\delta_4 . \quad (26)$$

The sub-case $2/5 \le m\cos\vartheta \le m_{\max}\cos\vartheta$ (gray area in Fig. 4) is depicted in diagram ❸ of Fig. 5. In this case $\tilde{i}_{pp}$ can be evaluated considering the switch configurations 11111, 11101, and 11001 with the corresponding application intervals $t_0/2$, t_4, and t_3, leading to

$$\tilde{i}_{pp} = \frac{2}{L}\left\{ m V_{dc} \cos\vartheta \frac{t_0}{2} + \left(m V_{dc} \cos\vartheta - \frac{V_{dc}}{5} \right) t_4 + \right. \\ \left. + \left(m V_{dc} \cos\vartheta - \frac{2V_{dc}}{5} \right) t_3 \right\}. \quad (27)$$

The corresponding normalized current ripple is

$$r(m,\vartheta) = m\cos\vartheta\,\delta_0 + 2\left(m\cos\vartheta - \frac{1}{5} \right)\delta_4 + 2\left(m\cos\vartheta - \frac{2}{5} \right)\delta_3 \quad (28)$$

2) Evaluation in the second sector

Considering sector ②, $\pi/5 \le \vartheta \le 2\pi/5$, three different sub-cases can distinguished: $0 \le m\cos\vartheta \le 1/5$, $1/5 \le m\cos\vartheta \le 2/5$, and $2/5 \le m\cos\vartheta \le m_{\max}\cos\vartheta < 3/5$. All these sub-cases are represented in Fig. 6.

The sub-case $0 \le m\cos\vartheta \le 1/5$ (yellow area in Fig. 4) is depicted in diagram ❶ of Fig. 6. According to this figure, $\tilde{i}_{pp}$ can be evaluated by (8), (9) and (21) considering the switch configurations 00000 and 01000 with corresponding application intervals $t_0/2$ and t_4

$$\tilde{i}_{pp} = \frac{2}{L}\left\{ m V_{dc} \cos\vartheta \frac{t_0}{2} + \left(m V_{dc} \cos\vartheta + \frac{1}{5} V_{dc} \right) t_4 \right\}. \quad (29)$$

Normalizing as in (23) and introducing the duty-cycles, the normalized current ripple becomes

$$r(m,\vartheta) = m\cos\vartheta\,\delta_0 + 2\left(m\cos\vartheta + \frac{1}{5} \right)\delta_4 , \quad (30)$$

The sub-case $1/5 \le m\cos\vartheta \le 2/5$ is depicted in diagram ❷ of Fig. 6. There are two possible situations for evaluating $\tilde{i}_{pp}$, corresponding to the yellow-green areas of sector ② in Fig. 4:
- in the first situation, yellow area, (solid orange line in Fig. 6), $\tilde{i}_{pp}$ can be determined as in previous sub-case by considering switch configurations 00000 and 01000 with corresponding application intervals $t_0/2$ and t_4, leading to (29) and (30);
- in the second situation, green area (dashed orange line in Fig. 6), $\tilde{i}_{pp}$ can be determined by considering the switch configurations 11111 and 11101 with the corresponding application intervals $t_0/2$ and t_1, leading to

$$\tilde{i}_{pp} = \frac{2}{L}\left\{ m V_{dc} \cos\vartheta \frac{t_0}{2} + \left(m V_{dc} \cos\vartheta - \frac{1}{5} V_{dc} \right) t_1 \right\}. \quad (31)$$

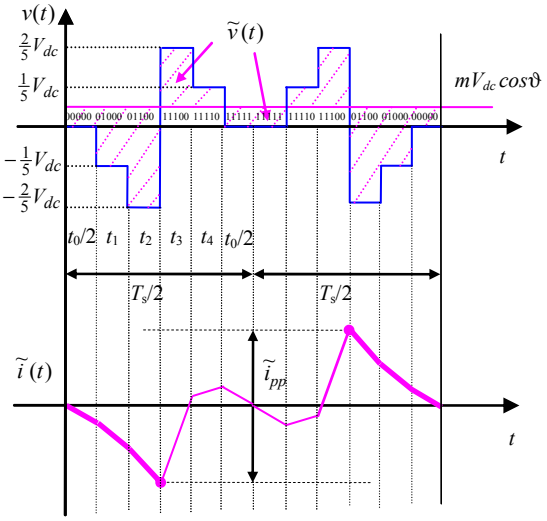

Fig. 7. Output voltage and current ripple in one switching period for sector ③, $2\pi/5 \le \vartheta \le \pi/2$.

The normalized current ripple is

$$r(m,\vartheta) = m\cos\vartheta\,\delta_0 + 2\left(m\cos\vartheta - \frac{1}{5} \right)\delta_1 . \quad (32)$$

The last sub-case $2/5 \le m\cos\vartheta \le m_{\max}\cos\vartheta$ (red area in Fig. 4) is depicted in diagram ❸ of Fig. 6. According to this figure, $\tilde{i}_{pp}$ can be evaluated considering the switch configurations 11111, 11101, and 11100 with the corresponding application intervals $t_0/2$, t_1, and t_2, leading to

$$\tilde{i}_{pp} = \frac{2}{L}\left\{ m V_{dc} \cos\vartheta \frac{t_0}{2} + \left(m V_{dc} \cos\vartheta - \frac{V_{dc}}{5} \right) t_1 + \right. \\ \left. + \left(m V_{dc} \cos\vartheta - \frac{2V_{dc}}{5} \right) t_2 \right\}. \quad (33)$$

The normalized current ripple is

$$r(m,\vartheta) = m\cos\vartheta\,\delta_0 + 2\left(m\cos\vartheta - \frac{1}{5} \right)\delta_1 + 2\left(m\cos\vartheta - \frac{2}{5} \right)\delta_2 \quad (34)$$

3) Evaluation in the third sector (half)

With reference to the half of sector ③, $2\pi/5 \le \vartheta \le \pi/2$ (blue area in Fig. 4), there are not sub-cases, and the only occurrence is $0 \le m\cos\vartheta \le m_{\max}\cos\vartheta < 1/5$, as depicted in Fig. 7. In this case, $\tilde{i}_{pp}$ can be evaluated by (8), (9) and (21), considering the switch configurations 00000, 01000, and 01100 with the corresponding application intervals $t_0/2$, t_1 and t_2, leading to

$$\tilde{i}_{pp} = \frac{2}{L}\left\{ m V_{dc} \cos\vartheta \frac{t_0}{2} + \left(m V_{dc} \cos\vartheta + \frac{1}{5} V_{dc} \right) t_1 + \right. \\ \left. + \left(m V_{dc} \cos\vartheta + \frac{2}{5} V_{dc} \right) t_2 \right\}. \quad (35)$$

Normalized current ripple is

$$r(m,\vartheta) = m\cos\vartheta\,\delta_0 + 2\left(m\cos\vartheta + \frac{1}{5} \right)\delta_1 + 2\left(m\cos\vartheta + \frac{2}{5} \right)\delta_2 . \quad (36)$$

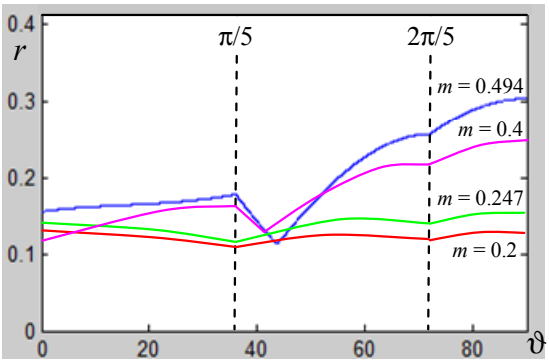

Fig. 8. Normalized peak-to-peak current ripple amplitude $r(m,\vartheta)$ for different modulation indexes in the phase angle range $\vartheta = [0, \pi/2]$.

D. *Peak-to-peak current ripple diagrams*

In order to show the behavior of the peak-to-peak current ripple amplitude in the fundamental period for all the possible cases, in Figs. 8 and 9 is represented the normalized function $r(m,\vartheta)$ defined by (23). Fig. 8 shows $r(\vartheta)$ for m = 0.2, 0.247, 0.4, and 0.494 (= 2 x 0.247), corresponding to the dashed circles in Fig. 4. The 3 ranges of ϑ correspond to the three sectors from ① to ③. The further sub-region in sector ② (green- and red-colored areas in Fig. 4) can be distinguished for m = 0.4. Fig. 9 shows the colored map of $r(m,\vartheta)$ for the first quadrant within the modulation limits. It can be noted that ripple amplitude is obviously zero for m = 0, since the null configurations are the only applied, increasing almost proportionally with m in the neighbourhoods of m = 0. A phase angle with minimum ripple can be identified, that is $\vartheta \approx 40°\div45°$, and a phase angle with maximum ripple, that is $\vartheta = 90°$, with ripple amplitude proportional to modulation index: $r(m, 90°) = 2/5[K_1+K_3]\, m \approx 0.616\, m$, resulting from (36). This aspect is further developed in the following sub-section.

E. *Maximum of the current ripple*

In order to estimate current ripple amplitude in the whole fundamental period, the maximum of the current ripple can be evaluated in the phase angle range [0, 90°]. For this purpose, two relevant angles can be observed in Figs. 8 and 9: a local maximum is for $\vartheta = 0°$, and a further local maximum is for $\vartheta = 90°$. In particular, to determine these two local maxima, it can be set $\vartheta = 0$ in (24), and $\vartheta = 90°$ in (36), introducing the application times given by (14) - (18). The maximum value of normalized peak-to-peak current ripple amplitude as a function of the modulation index becomes

$$r^{max}(m) = max\left\{ m\left[1-2mK_1{}^2-2mK_1K_3\right],\ \frac{2}{5}[K_1+K_3]m \right\}. \qquad (37)$$

The intersection between the two local maxima gives the border value of modulation index

$$m\left[1-2mK_1{}^2-2mK_1K_3\right] = \frac{2}{5}[K_1+K_3]m\,, \qquad (38)$$

leading to $m \approx 0.212$. Finally, combining (37) and (38), the maximum of the normalized current ripple is

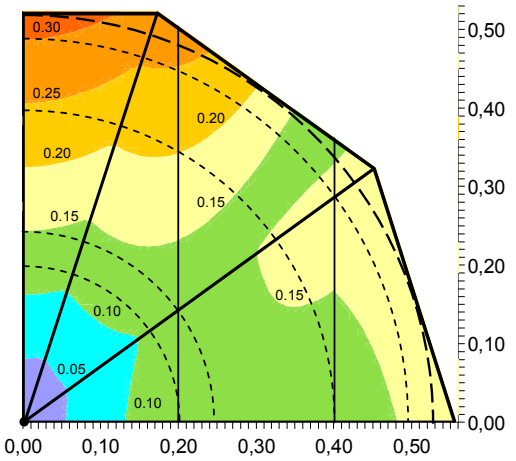

Fig. 9. Map of the normalized peak-to-peak current ripple amplitude $r(m,\vartheta)$

$$r^{max}(m) = \begin{cases} m\left[1-2mK_1{}^2-2mK_1K_3\right] & \text{for } m \le 0.212\,, \\ \dfrac{2}{5}[K_1+K_3]m & \text{for } m \ge 0.212\,. \end{cases} \qquad (39)$$

The composition of the two local maxima is given in Fig. 10, leading to the global maximum. The four white dots represent the specific points for m = 0.2, 0.247, 0.4, and 0.494, displayed in Fig. 8 and further examined in simulations. It can be noted that maximum function is almost linear with the modulation index, strictly for $m > 0.212$. Then, on the basis of (39) and (23), a simplified expression for maximum of peak-to-peak current ripple amplitude is obtained

$$\tilde{i}_{pp}{}^{max} = \frac{V_{dc}T_s}{5L}m[K_1+K_3] \cong \frac{V_{dc}T_s}{3.25\,L}m\,. \qquad (40)$$

III. NUMERICAL RESULTS

In order to verify the theoretical developments shown in previous sections, circuit simulations are carried out by SimPowerSystems (Matlab) considering a 5-phase VSI supplying a balanced RL load, having R = 7Ω and L = 3mH.

In all simulations the fundamental frequency f is set to 50 Hz, the switching frequency $1/T_s$ is 2 kHz, and the dc voltage supply V_{dc} is 100V. A centered symmetrical carrier-based PWM technique is considered, equivalent to the multiple space vector PWM presented in Section II. B.

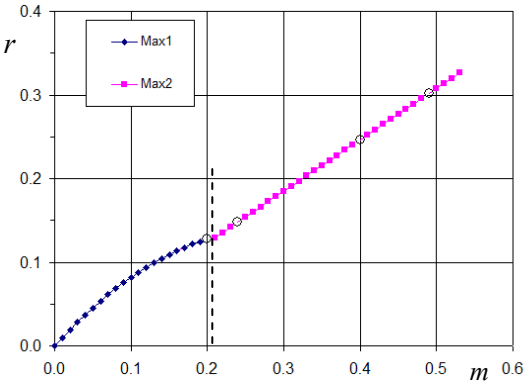

Fig. 10. Maximum of the normalized peak-to-peak current ripple amplitude as function of modulation index.

The instantaneous current ripple $\tilde{i}$ in simulations is calculated as the difference between the instantaneous current and its fundamental component, i.e.

$$\tilde{i}(t) = i(t) - I_{fund}(t). \quad (41)$$

The 5-phase system is well balanced and first phase is selected for further analysis, as in analytical developments. Different values of m are investigated (0.2, 0.247, 0.4, and 0.494 = 2x0.247), as in Section II, to cover all the possible cases.

In Figs. 11, 13, 15, and 17 the current ripple $\tilde{i}$ calculated in simulations by (41) (blue trace) is compared with the half of peak-to-peak current ripple, $\tilde{i}_{pp}/2$, evaluated in the different regions by the equations presented in Section II. C (red trace), for one fundamental period. Figures present different cases simulated with the different modulation indexes. Each figure is backed with the enlarged detailed view of the current ripple.

In the corresponding Figs. 12, 14, 16, and 18 is depicted the instantaneous output current with the calculated upper/lower ripple envelope, depicted in blue/red colors, respectively.

The agreement is good in the whole fundamental. Shown figures (Fig. 11 to Fig. 18) are for modulation indexes that cover almost all possible sub-cases (colored regions from Fig. 4). This proves the validity of the derived analytical equations.

IV. CONCLUSION

In this paper the instantaneous output current ripple in 5-phase PWM inverters has been identified and analyzed in details. In particular, the analytical expression of peak-to-peak current ripple amplitude has been derived in the whole fundamental period as function of the modulation index by identifying three different relevant cases and some sub-cases.

Furthermore, a simplified expression to evaluate maximum of the current ripple amplitude in the fundamental period is given. In particular, it has been pointed out that maximum peak-to-peak current ripple amplitude is almost linear function of the modulation index. The analytical developments have been verified with numerical simulations with reference to four relevant cases by a realistic circuit model.

Despite of the proposed analysis is based on centered symmetrical PWM, it can be easily extended to either discontinuous or asymmetrical modulation, both carrier-based and space vector PWM. Furthermore, the derived analytical expressions can be utilized to minimize the current ripple amplitude by properly adjusting the switching frequency and/or by modifying the sharing of application time of the null-voltage-vector between the two null switch configurations.

REFERENCES

[1] H.A. Toliyat, S.P. Waikar, T.A. Lipo, "Analysis and simulation of five-phase synchronous reluctance machines including third harmonic of airgap MMF," *IEEE Trans. on Industry Applications*, vol.34, no. 2, pp. 332-339, March/April 1998.

[2] H. Xu, H.A. Toliyat, L.J. Petersen, "Five-phase induction motor drives with DSP-based control system," *IEEE Trans. on Power Electronics*, vol. 17, No. 4, pp. 524-533, July 2002.

[3] H.M. Ryu, J.K. Kim, S.K. Sul, "Synchronous frame current control of multi-phase synchronous motor. Part I. Modelling and current control based on multiple d-q spaces concept under balanced condition," Proc. 39th IAS Annual Meeting, 3-7 October 2004, vol. 1, pp. 56-63.

[4] L. Parsa, H.A. Toliyat, "Five-phase permanent-magnet motor drives," *IEEE Trans. on Industry Applications*, vol. 41, no. 1, pp. 30-37, Jan./Febr. 2005.

[5] G. Grandi, G. Serra, A. Tani, "General analysis of multi-phase systems based on space vector approach," Proc. of 12th Power Electronics and Motion Control Conference , EPE-PEMC, Portoroz (Slovenia), Aug. 30 - Sept. 1, 2006.

[6] H.M. Ryu, J.W. Kim, S.K. Sul, "Analysis of multi-phase space vector pulse width modulation based on multiple d-q spaces concept," *IEEE Trans. on Power Electronics*, Vol. 20, No. 6, pp. 1364-1371, Nov. 2005.

[7] A. Iqbal, E. Levi, "Space vector modulation schemes for a five- phase voltage source inverter," Proc. of European Power Electronic Conference , EPE, Sept. 11-14, 2005, Dresden (D), pp. 1-12.

[8] P.S.N. de Silva, J.E. Fletcher, B.W. Williams, "Development of space vector modulation strategies for five phase voltage source inverters," Proc. of Power Electronics, Machines and Drives Conference, PEMD, March 31 – April 2, 2004, vol. 2, pp. 650-655.

[9] O. Ojo, G. Dong, "Generalized Discontinuous Carrier-Based PWM Modulation Scheme for Multi-Phase Converter-Machine Systems," Proc. of 40th Annual Meeting, IEEE Industry Applications Society, Oct. 2-6, 2005, Hong Kong, pp. 1374-1381.

[10] A. Iqbal and S. Moinuddin, "Comprehensive relationship between carrier-based PWM and space vector PWM in a five-phase VSI,", *IEEE Trans. on Power Electronics*, vol.24, no.10, 2009, pp. 2379-2390.

[11] D. Casadei, M. Mengoni, G. Serra, A. Tani, L. Zarri "A new carrier-based PWM strategy with minimum output current ripple for five-phase inverters," Proceedings of the 14th European Conference on Power Electronics and Applications, EPE, Aug. 30 -Sept. 1, 2011, pp. 1-10.

[12] D. Dujic, M. Jones, E. Levi, "Analysis of output current ripple rms in multiphase drives using space vector approach," *IEEE Trans. on Power Electronics*, vol. 24, no. 8, August 2009, pp. 1926-1938.

[13] M. Jones, D. Dujic, E. Levi, J. Prieto, F. Barrero "Switching ripple characteristics of space vector PWM schemes for five-phase two-level voltage source inverters-Part2: Current ripple," *IEEE Trans. on Industrial Electronics*, vol. 58, no. 7, July 2011, pp. 2799-2808.

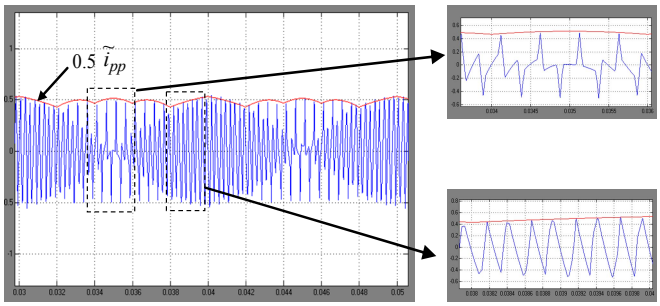

Fig. 11. Current ripple for m = 0.2: simulation results (blue) and evaluated peak-to-peak amplitude (red envelope) in fundamental period, with details.

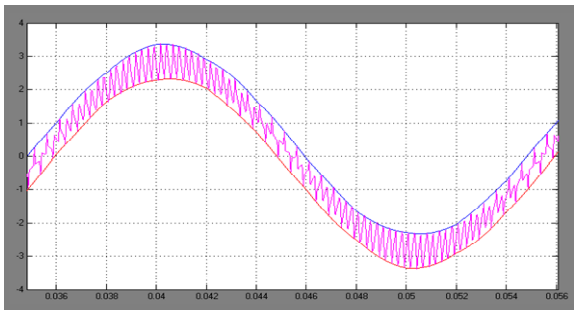

Fig. 12. Instantaneous output current with calculated ripple envelopes (red and blue traces) for m = 0.2.

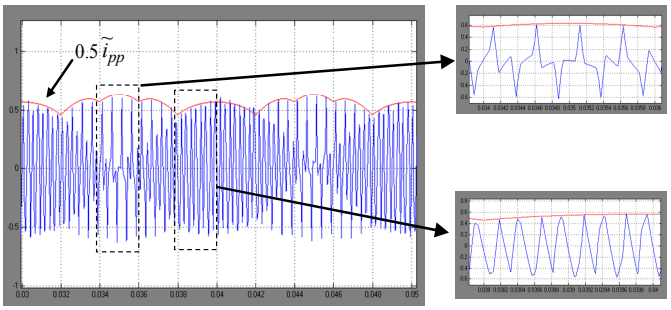

Fig. 13. Current ripple for m = 0.247: simulation results (blue) and evaluated peak-to-peak amplitude (red envelope) in fundamental period, with details.

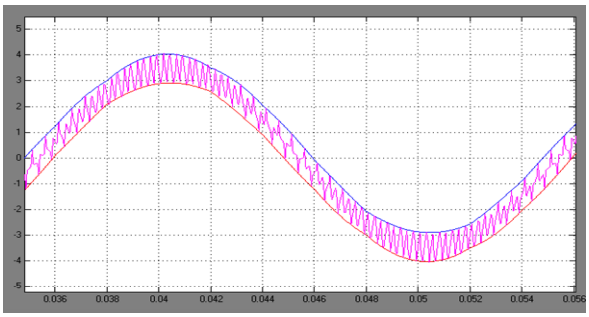

Fig. 14. Instantaneous output current with calculated ripple envelopes (red and blue traces) for m = 0.247.

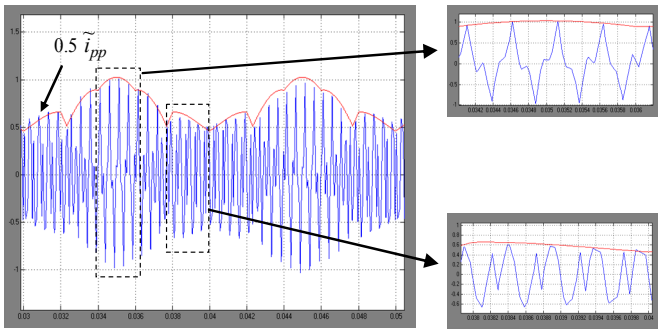

Fig. 15. Current ripple for m = 0.4: simulation results (blue) and evaluated peak-to-peak amplitude (red envelope) in fundamental period, with details.

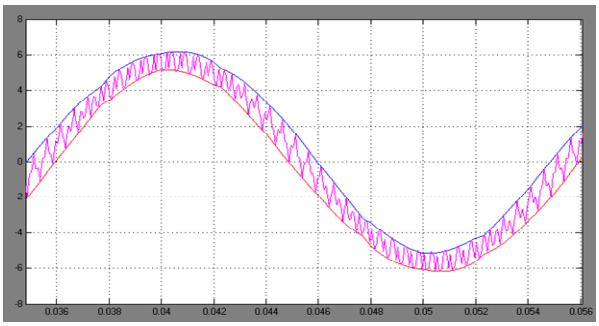

Fig. 16. Instantaneous output current with calculated ripple envelopes (red and blue traces) for m = 0.4.

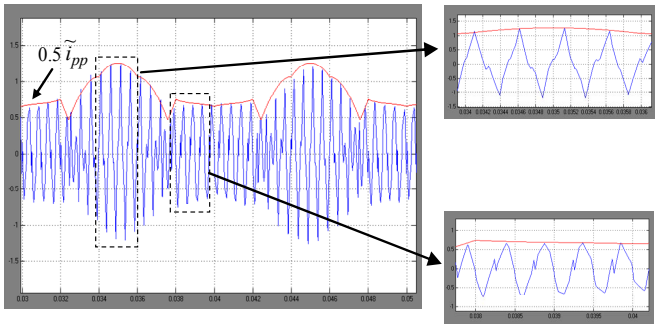

Fig. 17. Current ripple for m = 0.494: simulation results (blue) and evaluated peak-to-peak amplitude (red envelope) in fundamental period, with details.

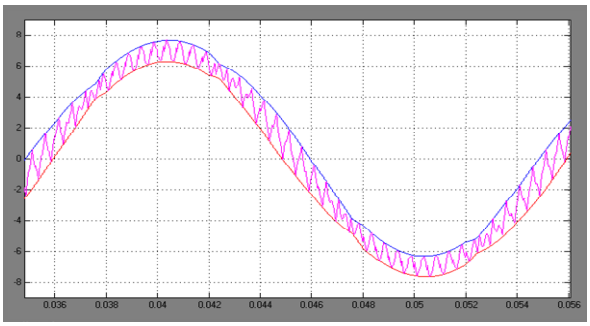

Fig. 18. Instantaneous output current with calculated ripple envelopes (red and blue traces) for m = 0.494.

[14] P.A. Dahono, Deni, E.G. Supriatna,"Output current-ripple analysis of five-phase PWM inverters," *IEEE Trans. on Industry Applications*, vol. 45, no. 6, Nov/Dec 2009, pp. 2022-2029.

[15] D. Dujic, M. Jones, E. Levi, "Analysis of output current-ripple RMS in multiphase drives using polygon approach," *IEEE Trans. on Power Electronics*, vol. 25, no. 7, July 2010, pp. 1838–1849.

[16] D. Jiang, F. (Fred) Wang "Study of analytical current ripple of three-phase PWM converter," Applied Power Electronics Conference and Exposition, APEC, 2012 Twenty-Seventh Annual IEEE, 5-9 Feb. 2012, pp. 1568 - 1575 .

[17] G. Grandi, J. Loncarski, "Evaluation of current ripple amplitude in three-phase PWM voltage source inverters," 8th Int. Conference-Workshop Compatibility and Power Electronics , CPE, 5-7 June 2013.

[18] G. Grandi, J. Loncarski, R. Seebacher "Effects of current ripple on dead-time distortion in three-phase voltage source inverters," 2nd IEEE ENERGYCON Conference & Exhibition, 2012 / Advances in Energy Conversion, Florence, Italy, 9-12 Sept. 2012.

[19] M.A. Herran, J.R. Fischer, S.A. Gonzalez, M.G. Judewicz, , D.O. Carrica, "Adaptive dead-time compensation for grid-connected PWM inverters of single-stage PV systems," *IEEE Transaction on Power Electronics*, vol.28, no.6, June 2013, pp. 2816-2825.

[20] J. Schellekens, R. Bierbooms, and J. Duarte, "Dead-time compensation for PWM amplifiers using simple feed-forward techniques," in Proc. of XIX Int. Conf. Electr. Mach., Sep. 2010, pp. 1–6.

[21] X. Mao, R. Ayyanar, H. k. Krishnamurthy, "Optimal variable switching frequency scheme for reducing switching loss in single-phase inverters based on time-domain ripple analysis," *IEEE Trans. on Power Electronics*, vol.24, no.4, April 2009, pp. 991-1001

[22] C. Ngai-Man Ho, V.S.P. Cheung, and H. Shu-Hung Chung, "Constant-frequency hysteresis current control of grid-connected VSI without bandwidth control," *IEEE Trans. on Power Electronics*, Vol. 24, No. 11, Nov. 2009.

[23] D.G. Holmes, R. Davoodnezhad, and BP. McGrath, "An improved three-phase variable-band hysteresis current regulator," *IEEE Trans. on Power Electronics*, Vol. 28, No. 1, Jan. 2013, pp. 441–450.

[24] E. Levi, D. Dujic, M. Jones, G. Grandi, "Analytical determination of DC-bus utilization limits in multi-phase VSI supplied AC drives," *IEEE Trans. on Energy Convers*, vol. 23, no. 2, June 2008, pp. 433-443.